This is a repository copy of *Surface Polymerization and Controlled Pyrolysis: Tailorable Synthesis of Bumpy Hollow Carbon Spheres for Energy Storage*.

White Rose Research Online URL for this paper:
https://eprints.whiterose.ac.uk/172594/

Version: Accepted Version

Surface Polymerization and Controlled Pyrolysis: Tailorable Synthesis of Bumpy Hollow Carbon Spheres for Energy Storage

Qianyi Tao, [‡a] *Zhifeng Zhu,* [‡a] *Sunjie Ye,* [b] *Gaojian Lin,* [c] *Hui Chen,* [a] *Yingfeng Tu,* [a] *guanghui Bai,* [d] *Lu Zhang,* [d] *and Xiaoming Yang* [*a]

a State and Local Joint Engineering Laboratory for Novel Functional Polymeric Materials, Suzhou Key Laboratory of Macromolecular Design and Precision Synthesis, Department of Polymer Science and Engineering, College of Chemistry, Chemical Engineering and Materials Science, Soochow University, Suzhou 215123, P. R. China.

b School of Physics and Astronomy, University of Leeds, LS2 9JT, Leeds, UK.

c Department of Mechanics Engineering, School of Mechatronical Engineering, Beijing Institute of Technology, Beijing 100081, China

d Science and Technology on Space Physics Laboratory, No.1, nandahongmen Road, Fengtai District, Beijing 100076, China

‡ These two authors contributed equally to this work.

*Corresponding author. Tel: +86 65882130. E-mail: yangxiaoming@suda.edu.cn

ABSTRACT Architectural design of hollow carbon spheres (HCSs) plays a vital role in improving their performance and expanding applications. The tailorable synthesis of bumpy or asymmetric HCSs with a refined structure remains a challenge. Herein, bumpy hollow carbon spheres (BHCSs) and bumpy concave hollow carbon spheres (BCHCSs) have been engineered. The synthesis involves the formation of core/shell precursor via the surface polymerization of pyrrole monomers on polystyrene nanoparticles, followed by the controlled pyrolysis process under different conditions. In comparison with HCSs, the concave hollow structure can reduce the excessive interior cavity and maintain prevalent merits of hollow structures; The bumpy shell can improve the surface area and number of active sites thus improving the kinetics as energy storage devices. As a result, among BCHCSs, BHCSs and HCSs, BCHCSs exhibit optimal electrochemical performance. The lithium-ion hybrid capacitors (LICs) employing BCHCSs as anode can deliver the energy density of 0.2182 KWh kg^{-1} at a power density of 0.2235 KW Kg^{-1}. Overall, this study provides an innovative design and strategy for constructing unique carbon nano-architectures for energy storage.

Introduction

Carbon spheres and other nano carbon materials have shown great potential in the application of energy storage for their excellent electronic conductivity, high specific surface area, alongside stable electrochemistry [1-9]. The architectural design of carbon spheres endows them with a number of novel attributes including adjustable particle size distribution, regular geometry and refined structure, and hence of significant impact on their electric properties and corresponding

electrochemical performances [10-13]. Recently, numerous efforts have been dedicated to the engineering of hollow carbon spheres (HCSs) as energy storage electrode materials [14-19], because (i) the hollow cavity can provide free space favoring strain relaxation, as well as accommodation of volume change for electrode materials amid repeated lithium intercalation/deintercalation; (ii) the thin and porous shells can shorten diffusion distances for both electrons and lithium ions thus contributing to improved rate capability. However, low tap density, small specific surface area (SSA) and excessive interior cavity space of intact hollow structure hinder their application as energy storage electrodes. In addition to the merits of HCSs, hierarchical bumpy structure can increase SSA and enrich active sites, while buckled structures can decrease the redundant interior cavity space, increase the density of volumetric packing, and promote mass transport capabilities by shortening diffusion pathway [19-22]. However, the preparation of HCSs with a bumpy shell remains underdeveloped, let alone HCSs combining a bumpy shell and a concave cavity.

In this study, bumpy concave hollow carbon spheres (BCHCSs), and bumpy hollow carbon spheres (BHCSs) were fabricated by surface polymerization and controlled pyrolysis. The formation mechanism of the BCHCSs and BHCSs was investigated and discussed. The effects of architecture of the BCHCSs, BHCSs and HCSs on the energy storage performance were studied in detail. As the anode of lithium-ion hybrid capacitors (LICs), the LICs with BCHCSs can deliver a high energy density as 0.2182 KWh kg^{-1} and the power density as high as 0.2235 KW kg^{-1}. These outcomes suggest that architectural design of BCHCSs provides an effective route towards high-performance LICs.

Experimental Section

3

Materials. The styrene (Acros, 99%) and pyrrole (Aldrich, 99%) monomers were distilled under reduced pressure to remove the inhibitor and oligomer. Activated carbon (3000 m^2/g) was purchased from Beijing Carbon Century Technology Co., Ltd. Ferric chloride ($FeCl_3$, 98%), hydrochloric acid (A.R.), polyvinylpyrrolidone (PVP, Mw:1300000), ethanol (A.R.), polyvinylidene fluoride (PVDF), N-methyl 2-pyrrolidone (NMP), and carbon black were all purchased from Sinopharm Chemical Reagent Co and used as received.

Preparation Production

Preparation of PS NPs. 58 mg sodium chloride and 58 mg potassium persulfate were dissolved in 90 g of deionized water. After that, 8 ml of styrene monomer was dropped to the solution, which was bubbled with nitrogen for 15 min. and heated to 80 degree to react for 12 h. Oligomers and inorganic salts were purified by dialysis for one week. The obtained PS NPs showed a diameter of 580 ± 19.5 nm.

Preparation of PS@PVP@PPy core-shell NPs. 0.1 g PVP and 0.5 g PS NPs were dispersed in 35 mL of deionized water, then 0.534 g Py monomer and 2.7 g $FeCl_3 \cdot 6H_2O$ were added in the solution. After 24 hours polymerization at 25 °C, the precipitates were centrifuged, washed by deionized water and dried at 75 °C. PS@PPy nanoparticles in the absence of PVP were fabricated by the same steps.

Preparation of hollow carbon spheres (HCSs) bumpy concave hollow carbon spheres (BCHCSs) and bumpy hollow carbon spheres (BHCSs). The obtained PS@PVP@PPy NPs were thermal decomposed to synthesis BCHCSs and BHCSs in tubular furnace under inert gases and in vacuum, respectively. The obtained PS@PPy NPs without PVP were also carbonized to obtain HCSs in a

quartz tubular furnace under nitrogen atmosphere. The product was heated up to 950 °C at a heating rate of 10 °C/min, held at 950 °C for 2 h and then cooled to room temperature.

Results and discussion

Material synthesis and mechanism discussion

The fabrication process of BHCSs, and BCHCSs and HCSs is schematically described in **Figure 1**a. The polyvinylpyrrolidone (PVP) modified polystyrene (PS) hard core and PPy shell nanoparticles (NPs) were prepared at first [23]. Then BCHCSs and BHCSs were obtained by pyrolysis of PS@PVP@PPy core/shell precursor under nitrogen atmosphere and in vacuum, respectively.
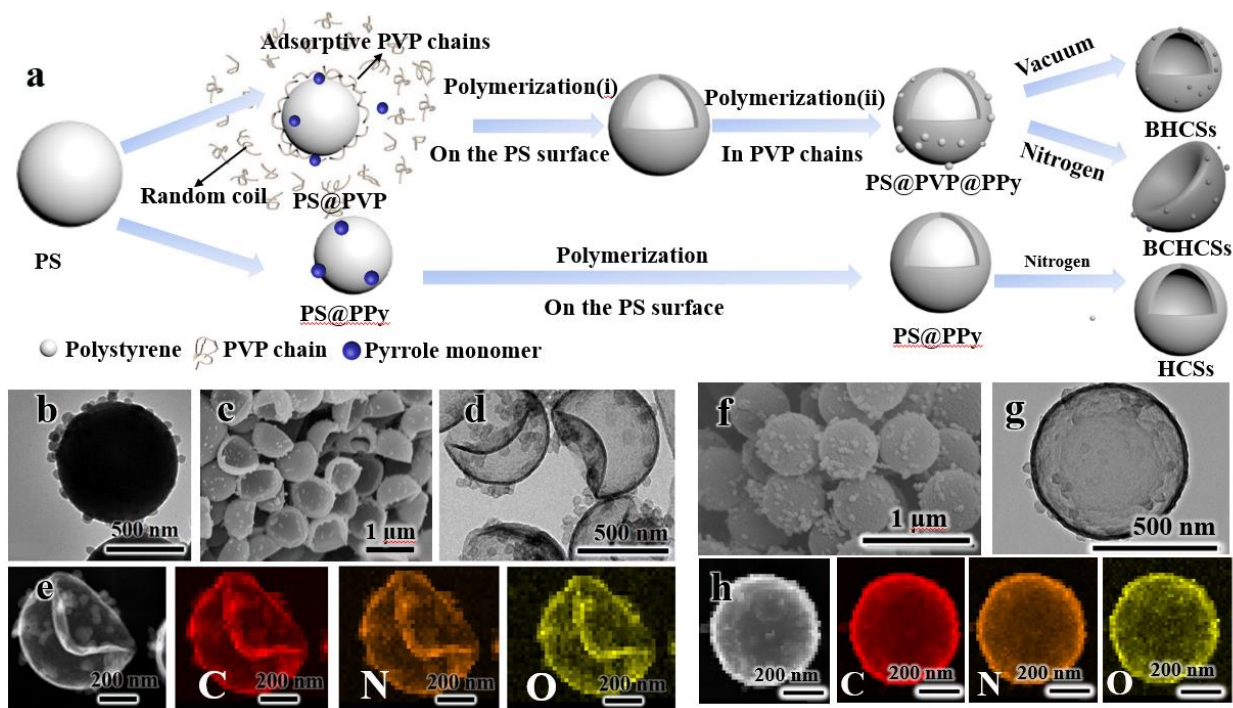
Figure 1. (a) Schematic depiction of the fabrication process of HCSs, BHCSs, and BCHCSs. (b) TEM image of bumpy PS@PVP@PPy core/shell particles; SEM images of BCHCSs (c) and

5

BHCSs (f); TEM image of BCHCSs (d) and BHCSs (g); HAADF-STEM image and corresponding element mapping of C, N and O in an individual BCHCSs (e) and BHCSs (h).

The transmission electron microscopy (TEM) image of PS@PVP@PPy core/shell NPs demonstrated bumpy shell (**Figure 1**b). The formation mechanism will be discussed in detail below. After pyrolysis under nitrogen atmosphere or in vacuum, bumpy shell was inherited for both BCHCSs and BHCSs while PS core was removed completely (**Figure 1**c–g). Interestingly, the pyrolysis under nitrogen atmosphere yielded concaved structure, while that under vacuum condition yielded non-concaved structure (**Figure 1**c–g). The high-angle annular dark-field-scanning transmission electron microscopy (HAADF-STEM) images in **Figure 1**e and h confirm the even distribution of C, N, O elements of both BCHCSs and BHCSs. It is worth noting that smooth core/shell precursor and corresponding HCSs were obtained without PVP modification layer (Figure S1a and S1b), suggesting that PVP chains show an essential part in the formation of bumpy and concave shell.

To investigate the formation mechanism of bumpy PS@PVP@PPy core/shell NPs, polymerization dynamics were investigated by SEM imaging at different time points during reaction (**Figure 2**a–h). It can be observed from **Figure 2**a that the surface of PS NPs is smooth with a particle diameter of 580 nm. With increasing the reaction time to 40 min, the particle size increases to 750 nm (**Figure 2**e), indicating the rapid polymerization of pyrrole monomers on the PS NPs surface. After 40 min, the polymerization rate on the surface of PS NPs decreased sharply while small PPy dots with diameter about 45 nm appeared (**Figure 2**e–h). It can be concluded that there are two stages of growth of pyrrole on the surface of PS particles in the presence of adsorption PVP layer (**Figure** 2i). The maximum theoretical adsorption PVP chains on the surface of 0.5 g PS NPs with a particle size of 580 nm was about 0.00345 g according to the literature, which was

attributed to the formation of smooth PPy shell at the first polymerization stage [24]. However, 0.1 g PVP chains were used in this study, the excess PVP chains were located around the PS NPs as random coils (**Figure 1**a) [24], as confirmed by the results of dynamic light scattering (DLS) (**Figure 2**j). After absorption of PVP chains, the diameter of PS NPs increased from 580 nm to 780 nm and the polydispersity index (PDI) increased from 0.040 to 0.085, indicating that absorbed PVP chains were located around the PS NPs. The coils of PVP chains provided the nucleation sites for the PPy dots to initiate the second polymerization stage, contributing to the formation of bumpy shell.
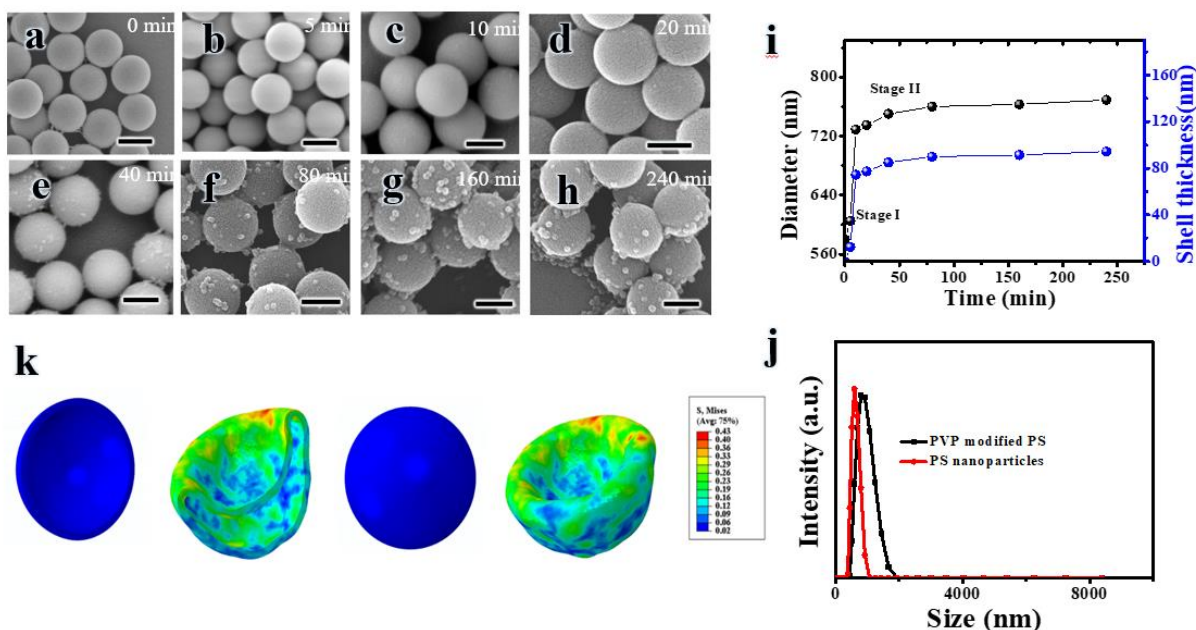
Figure 2. SEM images of PS@PVP@PPy core/shell NPs obtained after different reaction time: (a) 0 min; (b) 5 min; (c) 10 min; (d) 20 min; (e) 40 min; (f) 80 min; (g) 160 min; (h) 240 min. (The scale bar is 500 nm) (i) Curve plot of reaction time versus particle size (nm) and shell thickness (nm). (j) the diameter of PS NPs and PVP modified PS NPs characterized by dynamic light scattering. (k) Cross-sectional view and isometric view of FE simulation of a single bumpy hollow particles subjected to external pressure.

BCHCSs were prepared by controlled pyrolysis precursor to 950 °C in inert gas, during which PS chains were completely decomposed to form vacuum in the core, while PPy shells were carbonized and deformed at the same time, due to the pressure difference between purged nitrogen atmosphere and vacuum core. However, BHCSs without deformed structure were obtained by pyrolysis of bumpy core/shell precursor under vacuum. It can be concluded that the pressure provided by purged inert atmosphere is crucial for the deformation of shell (**Figure 1**a). For the sake of further figure out the mechanism of deformation process, we performed modelling on the buckling of a bumpy hollow particles by applying the external pressure loading on the surface of spherical shell through finite element (FE) simulation. **Figure 2**k shows the cross-sectional and isometric view of FE simulation of a single hollow particles. According to the simulation results, a critical buckling loading about 7.5 MPa was obtained.

Structure characterization
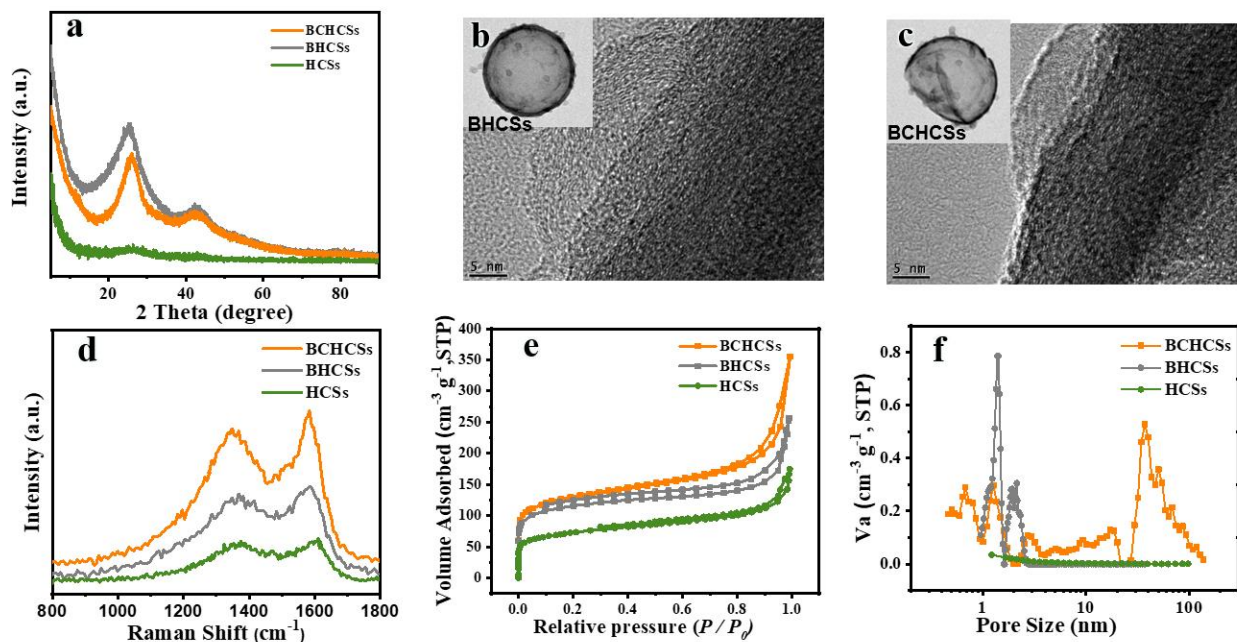
Figure 3. (a) XRD patterns of HCSs, BHCSs, and BCHCSs. HRTEM image of (b) BHCSs and (c) BCHCSs. (d) Raman spectra of HCSs, BHCSs, and BCHCSs. (e) N_2 adsorption isotherm of HCSs, BHCSs, and BCHCSs. (f) Pore size distributions of HCSs, BHCSs, and BCHCSs.

Figure 3a shows XRD patterns of HCSs, BHCSs, and BCHCSs samples. All samples exhibit broad peaks associated with (002) diffraction, indicating the amorphous nature of carbon materials [25,26]. High-resolution TEM (HRTEM) images of BCHCSs and BHCSs demonstrated the amorphous structure with slightly order graphite domain for both shell and attached dots (**Figure 3**b and c) [27,28]. These results show that the pyrolysis condition does not affect the crystalline phase of carbon spheres.

Raman spectra (**Figure 3**d) displayed the characteristic of sp^2 and sp^3 domains. The peak at 1350 cm^{-1} is assigned to D band corresponding to disordered carbon or defective graphitic structures, while the peak at 1600 cm^{-1} is assigned to G band corresponding to the graphitic layers and the tangential vibration of the carbon atoms. The I_G/I_D ratio is 1.07, 1.09 and 1.07 for HCSs, BCHCSs, and BHCSs, respectively, indicating that all samples have a low G-to-D band ratio, demonstrating the disordered carbon structure, in accordance with XRD results [29,30]. Amorphous carbon materials can deliver excellent ion diffusion kinetics for LICs anode owing to enhancement of capacitive charge-storage capabilities for the anode of Li ion storage.

The SSA of HCSs, BCHCSs, and BHCSs is 257, 466 and 423 m^2 g^{-1}, respectively (**Figure 3**e and **Table S**1). A typical IV-type adsorption curves was observed for all samples[31]. Pore structure parameters are listed in Table S1 and Figure 3f. BCHCSs exhibit the highest SSA, a hierarchically porous feature and a wide distribution in range from 2 to 100 nm, demonstrating abundant micropores, mesopores, and macropores due to the bumpy surface. BHCSs exhibit moderate SSA

and a narrow pore size distribution from 1 to 5 nm due to the vacuum pyrolysis condition. However, HCSs exhibits lowest SSA and scarce pores structure. It is envisaged that, the hierarchical porosity of BCHCSs will benefit their uses as anode materials, by facilitating the adsorption of lithium ions, the infiltration and transmission of electrolyte, and improving the mass transmission capacity.
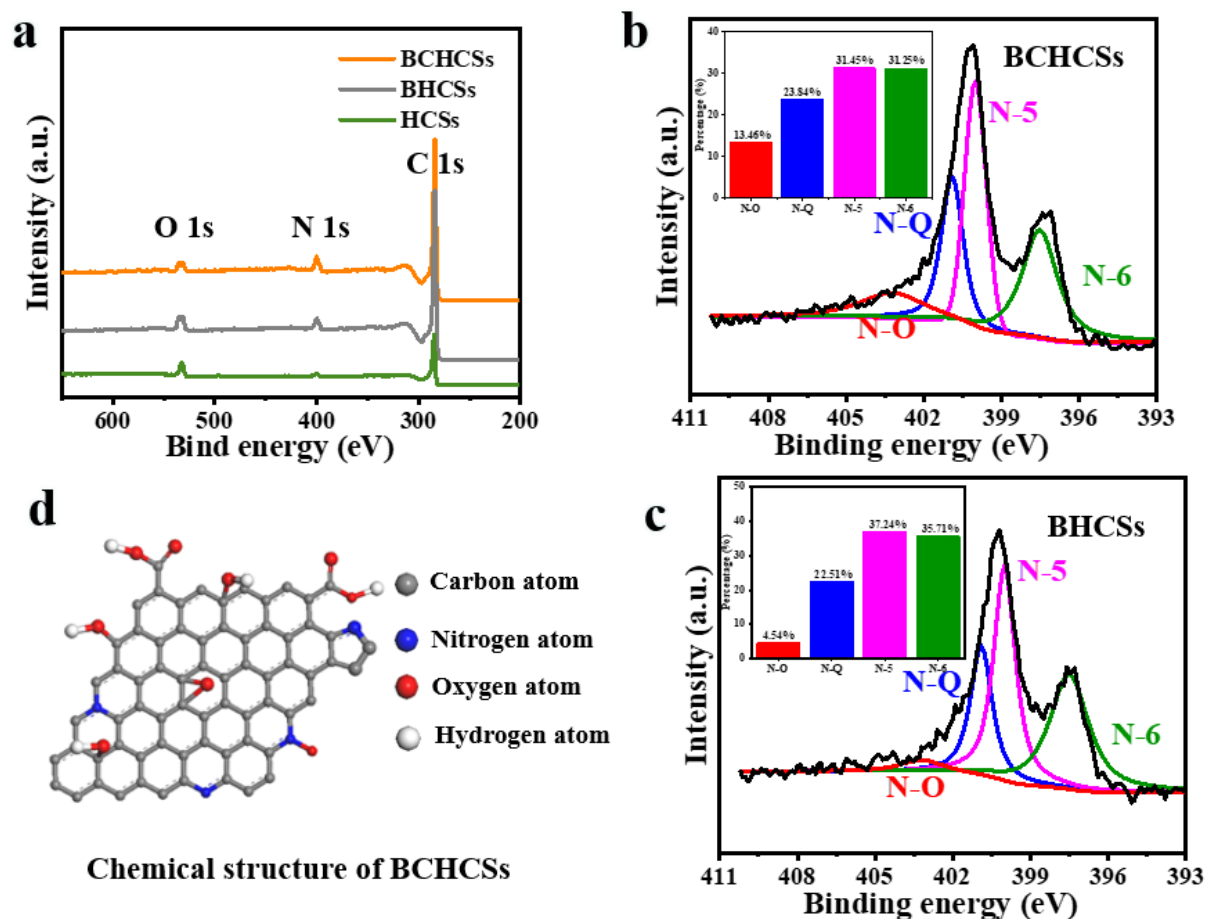
Figure 4. (a) Overall spectra of HCSs, BCHCSs, and BHCSs. Representative high-resolution N 1s XPS spectra of BCHCSs (b) and BHCSs (c). (d) schematic model of functional groups in DCHCSs.

The survey-scan XPS spectra clearly show three components indexing to C, N, and O (**Figure 4**a). The results of chemical composition (EA) elemental content (**Table S**1) suggest that BCHCSs exbibit the highest content of nitrogen 9.67% owing to the nitrogen containing precursor of PPy and PVP which can increase the conductivity of samples by improving the surface wettability [32,33]. The N 1s spectrum of BCHCSs (**Figure 4**b) and BHCSs (**Figure 4**b and c) is divided to four peaks, corresponding to graphitic nitrogen (N–Q), pyrrolic nitrogen (N–5), pyridinic nitrogen (N–6), and oxidized nitrogen (N–O). N–5 and N–6 have larger content than other nitrogen groups for both BCHCSs and BHCSs, implying the abundance of pyrrolic nitrogen and pyridinic nitrogen, which can boost electrochemical performance. It is acknowledged that, pyridinic–N and pyrrolic–N can amplify the specific capacitance of N-doped materials due to their pseudocapacitive contribution [34,35]. The results show that all samples have the same chemical formular (**Figure 4**d), suggesting that the pyrolysis condition has no effect on the chemical structure of the products.

Electrochemical analysis for half cells

The unique morphology, amorphous structure with slightly ordered graphite domain, high SSA, abundant pore structure, and heteroatoms of HCSs, BCHCSs and BHCSs made these carbon nanomaterials a promising candidate as energy storage electrodes. To assess the electrochemical properties of all samples, we constructed and tested half-cell configurations, by adopting coin-type cells having lithium foil as reference and counter electrodes. **Figure 5**a and b display a representative CV curve of BCHCSs and BHCSs anode at scan rates of 0.5 mV s^{-1} (potential range: 0.02–3.0 V vs Li/Li$^+$). As shown in **Figure 5**a and b, the sharp cathodic peak at around 0.14 V can be assigned to the step intercalation of lithium ions into porous carbon to yield Li–intercalated compound [36].
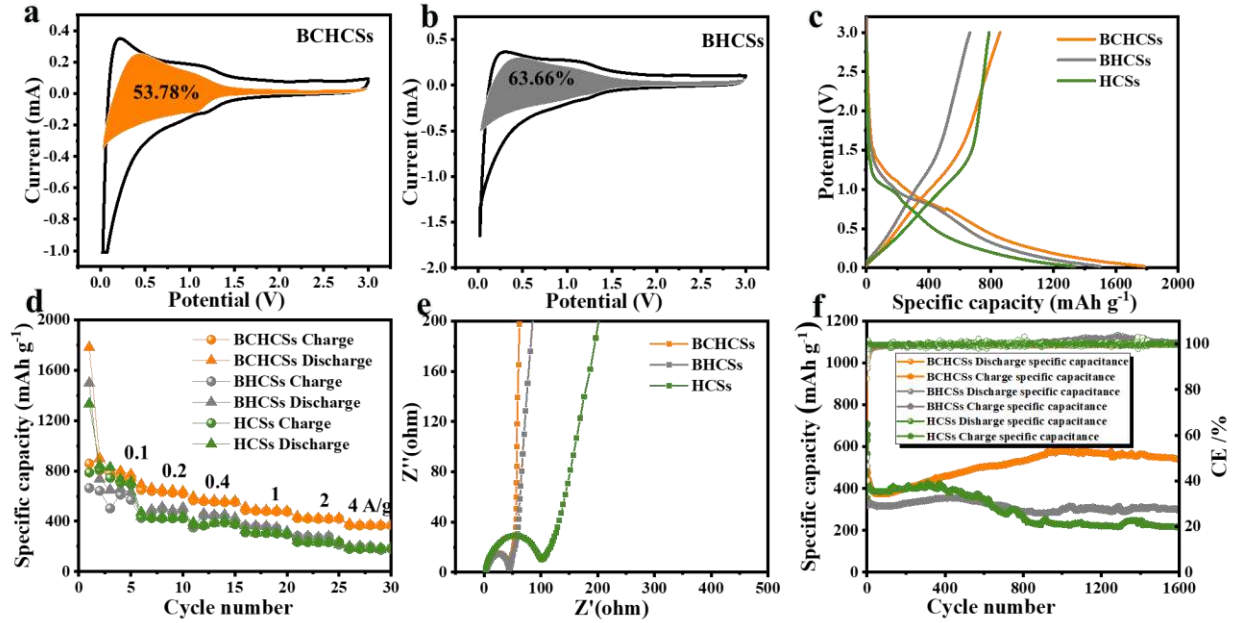
Figure 5. Electrochemical performance of BCHCSs and BHCSs based half-cell configurations: a representative CV curve of BCHCSs (a) and BHCSs (b) anode (potential range: 0.02-3.0 V vs Li/Li$^+$; scan rate: 0.5 mV s^{-1}). Area in shadow indicates the surface capacitive contribution as anode electrode; (c) Charge-discharge curves of BCHCSs, BHCSs and HCSs anode in the first cycle (current density: 0.1 A g^{-1}); (d) Rate performance of HCSs, BCHCSs and BHCSs anodes; (e) Nyquist plots of HCSs, BCHCSs and BHCSs electrodes; (f) Cycling stability and coulombic efficiency of BCHCSs, BHCSs and HCSs anode within 1600 cycles (current density: 2 A g^{-1}; mass loading: 0.41 mg cm^2.)

Based on the method of current separation, the contribution of capacitive capacity can be distinguished from the contribution of diffusion-controlled capacity as per the following equation as indicated by the shadowed area in the CV curve in **Figure 5**a and b [37-39].

$$i(V) = k_1 v + k_2 v^{1/2} \qquad (1)$$

12

where *i (V) represents* the response currents (*i*) corresponding to voltages (*V*). k_1 and k_2 are constants. k_1v and $k_2v^{1/2}$ represent capacitive effects and diffusion-controlled behavior, respectively. About 58.78% and 63.66% of the total current area (k_1v) arise from the contribution of the pseudocapacitive behavior at 0.5 mV s^{-1} for BCHCSs and BHCSs respectively, suggesting a capacity for rapid storage of Li$^+$ at high current density. These results show that the charge–storage of the BCHCSs and BHCSs electrode has two behaviors (capacitive capacity and diffusion-controlled capacity), desirable for rapid storage of lithium ions to balance kinetics of cathode.

Figure 5c depicts charge-discharge curves of the BCHCSs, BHCSs and HCSs anode in the first cycle. They exhibit sloping features similar to reported carbonaceous anodes, indicating the surface-driven dominated Li$^+$ storage behavior. The 1st cycle displays a specific capacity of 1783, 1498, and 1332 mAh g^{-1}, as well as a reversible specific capacity of 899,735 and 840 mAh g^{-1} for BCHCSs, BHCSs and HCSs anode, which is better than that of the capacity of graphite (372 mAh g^{-1}). The irreversible capacity results from the generation of SEI layer as well as the irreversible insertion of lithium ions at special sites in the carbon material [40,41]. Notably, the specific capacity of BCHCSs (1783 mAh g^{-1}) is approximately 4.8 folds of the theoretical capacity of graphite.

Figure 5d shows the rate performance of BCHCSs and BHCSs anode at different current densities. BCHCSs can deliver reversible capacities of 1783, 690.2, 593.8, 512.3, 439, 379.5 mA h g^{-1} at rates of 0.1, 0.2, 0.4, 1, 2, 4 A g^{-1}, respectively. While BHCSs and HCSs deliver lower capacities, demonstrating less good rate performance than that of BCHCSs. The unique architecture of BCHCSs retains the advantage of cavity structure thus reducing the charge transmission distance, and improving charge/electron transmission efficiency, which are confirmed by electrochemical impedance spectra (EIS) (**Figure 5**e). As can be seen from **Figure 5**e, the semicircles in high-frequency region reveal that, the BCHCSs and BHCSs electrodes

delivered the same charge-transfer impedance (Rct), while HCSs delivered higher Rct. These results suggest that, highly-efficient and rapid faradaic redox reactions take place at the electrode surface of BCHCSs and BHCSs. The slope line represents the Warburg impedance associated with solid-state Li^+ diffusion. However, the low frequency lines for BCHCSs and BHCSs are much steeper than that of HCSs, revealing much faster Li^+ diffusion. This improvement can be attributed to shorten diffusion pathway arising from the bumpy structure.

The cycling stability of BCHCSs, BHCSs and HCSs anode were measured at a current density of 2 A g^{-1}, and shown in **Figure 5**f. The charge and discharge process presents stability and reversibility, coupled with the coulombic efficiency (CE) of approximately 99.8% except in the initial stage. At the current density as high as 2 A g^{-1}, a capacity of 541.1 and 298.7 mAh g^{-1} was obtained for BCHCSs and BHCSs respectively, with nearly 100% coulombic efficiency following 1600 cycles (**Figure 5**f). These results suggest that BCHCSs feature large capacity, outstanding cycle lifespan and rate performance, thus holding great potential for carbon-based anode in high-performance LICs.

Electrochemical analysis for lithium-ion hybrid capacitors (LICs)

For developing asymmetric LICs of high performance, we have chosen commercial AC with an ultra–large SSA (3000 m^2/g) for carbon cathode. The electrochemical properties of cycling performances, discharge medium voltage, rate performances, and charge–discharge curves of AC half–cell were evaluated in Supporting Information. (**Figure S2** a–d). A novel LICs (BCHCSs//AC) is fabricated using the BCHCSs anode and AC cathode in the electrolyte of organic Li salt. Before the fabrication of the LICs, the anode of BCHCSs was subjected to a 70–

hour prelithiation for extending the potential window and eliminating the initial irreversible reactions. The stored charged of one electrode can be calculated on the basis of equation (2):

$$Q_{electrode} = m \times \Delta E \times C_{electrode} \quad (2)$$

$Q_{electrode}$ is the total charge, $C_{electrode}$ is the specific capacitance, m is the active mass, and ΔE is the potential window of each electrode. A mass balance of each electrode can be estimated based on equation (3) :

$$\frac{m_+}{m_-} = \frac{\Delta E \times C_{electrode-}}{\Delta E \times C_{electrode+}} \quad (3)$$

The best mass ratio of the anode to cathode was calculated to be about 1:6.5 [42]. The LICs device exhibits a wide working voltage window ranging from 0 to 4.5 V. **Figure 6**a schematically shows the proposed pathway for charge–storage during the charging process. Li$^+$ ions enter BCHCSs via several storage mechanisms, including interlayer insertion (graphite domain), adsorption onto nitrogen-containing active sites and carbon pores, faraday reactions of nitrogen to provide extra capacitive storage, and the accumulation PF_6^- ions on AC pores. The discharge process follows a reversed pathway of the charge process.

The electrochemical properties of the optimal LICs (BCHCSs//AC) are systematically studied. It can be seen from **Figure 6**b, the galvanostatic charge–discharge profiles at varying current densities assume a symmetric triangular shape, demonstrating good rate capability alongside high reversibility. The slightly distorted charge–discharge curves and CV curves (**Figure 6**c) arise from overlap of several charge–storage mechanisms. The corresponding IR drops (**Figure 6**d) indicate

a small polarization in charge–discharge processes [43], along with a low internal resistance that is favorable for thigh discharge power delivery in practical applications [44].
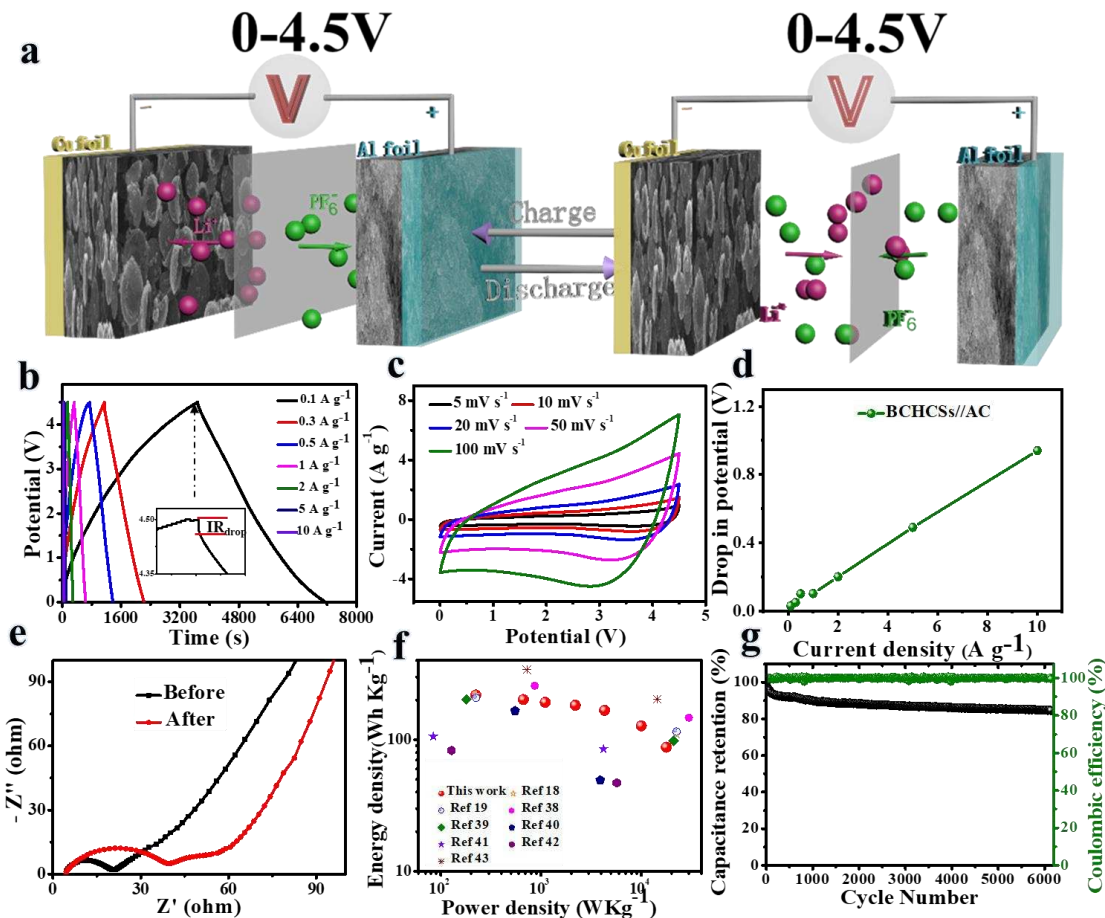
Figure 6. Electrochemical performance of BCHCSs//AC LICs (mass loading of BCHCSs to AC is 1:6.5). (a) Schematic depiction of the charge storage mechanism. (b) Galvanostatic charge-discharge curves at varying current densities. (c) Typical CV curves at varying scan rates (voltage range: 0–4.5 V) s. (d) IR drops at varying current densities for the fabricated LICs. (e) Nyquist plots of LICs before and after cycles. (f) Benchmarking of ragone plots with reported values. (g) Cycling stability at 4 A g^{-1}. Mass loading for anode and cathode is 0.42 mg/cm^2 and 2.73 mg/cm^2, respectively.

The IR drops appear at a dynamic state in the galvanostatic process which could cause the polarization resistance (**Figure 6**b), whereas EIS was measured at a static state of capacitors in which the polarization resistance was avoided [45]. The EIS curve of the LICs (**Figure 6**e) exhibits following features: (1) a small semicircle in the high–frequency area, revealing the capability of fast ion transport; (2) small deviations at middle-range frequencies, suggesting a low conductivity which may be caused by microporosity and pseudocapacitance, in accordance with the IR drops present in GCD measurements (**Figure 6**b); (3) a curve rising nearly vertically in the low–frequency range, displaying a typical capacitive behavior [46]. Taken together, these results demonstrate that microporous carbons can greatly boost electrochemical capacitance but impede the transport of ions, giving rise to charge–transfer resistance. The variation of EIS between LICs before and after cycling should be mainly caused by the effects the charge–transfer resistance, as reflected by semicircles observed in the high–frequency area.

According to the active substances of the two electrodes, we calculated energy density and power density relationship of the optimal LICs device. A maximum energy density of 218.2 Wh kg^{-1} is realized at a power density of 223.5 W kg^{-1} (**Figure 6**f). The comparison (**Table S**2 and **Figure 6**f) of the performance of our LICs with reported hybrid systems suggests that, our BCHCSs //AC LICs outperform previously reported LICs [47-51]. The superior energy density of power capability benefits from the unique architecture of anode material.

We also evaluated the cycling stability of our LICs (**Figure 6**g). At the current density of 4 A g^{-1}, the capacity remains 84.8% post 6000 cycles, with a coulomb efficiency nearly 100%. The key to realizing such a high rate and outstanding cycling stability lies in the architectural design of the nanomaterials in the anode, which allows rapid and reversible Li$^+$ storage and release to match the capacitive cathode. The BCHCSs have integrated mechanisms of intercalation/deintercalation and

absorption/desorption charge-storage to enable fast and durable Li^+ storage, which has greatly improved the anodic performance. Consequently, the two electrodes enjoy an optimal match in kinetic and lifespan, rendering the fabricated BCHCSs //AC LICs with desirable rate capability as well as great cycling stability.

Conclusions

In summary, we have successfully engineered BCHCSs and BHCSs, as well as elucidated their formation mechanism and outstanding electrochemical performance as anode for LICs. The architectural design of the carbon materials with high–level heteroatom–doping leads to enhanced contributions from capacitive chare–storage for anode. This effectively overcomes the electrochemical mismatch between anode of Li^+ storage and cathode of PF_6^- storage, enabling a BCHCSs //AC LICs. When the mass ratio of anode to cathode is 1:6.5 and the working voltage is in the range of 0.0 to 4.5V, the fabricated LICs can deliver the energy density of 218.2 Wh kg^{-1}at a power density of 223.5 W Kg^{-1}, which is higher than most reported work. This study provides new strategy for the architecture design of carbon nanostructures as high–performance anode materials to enhance the power and energy density of LICs.

Declaration of Competing Interest

The authors declare that they have no known competing financial interests or personal relationships that could have appeared to influence the work reported in this paper.

Supporting Information.

SEM and TEM images of HCSs; Pore structures, elemental composition, and lattice parameters of HCSs, BCHCSs, and BHCSs; Cycling stability of AC cathode; Corresponding discharge medium voltage of AC cathode; Rate performance of AC cathode; Charge−discharge curves of the AC cathode; comparison of reported LICs systems with BCHCSs//AC configuration; Characterization; FE Modeling; Electrochemical measurements.

Acknowledgment

REFERENCES

1. Xu, F.; Tang, Z.; Huang, S.; Chen, L.; Liang, Y.; Wu, D. et al. Facile synthesis of ultrahigh-surface-area hollow carbon nanospheres for enhanced adsorption and energy storage. Nat. Commun. 2015, 6, 7221-7230.

2. Liu, J.; Wickramaratne N.; Qiao, S.; Jaroniec, M. Molecular-based design and emerging applications of nanoporous carbon spheres. *Nat. Mater*. **2015**, 14, 763-774.

3. Zhao, T.; Elzatahry, A.; Li, X.; Zhao, D. Single-micelle-directed synthesis of mesoporous materials. *Nat. Rev. Mater*. **2019**, 4, 775-791.

4. Wang, X.; Feng, J.; Bai, Y.; Zhang, Q.; Yin, Y. Synthesis, Properties, and Applications of Hollow Micro-/Nanostructures. *Chem. Rev*. **2016**, 116, 10983−11060.

5. Bin, D.; Chi, Z.; Li, Y.; Zhang, K.; Cao, A.; Wan, L. et al. Controlling the Compositional Chemistry in Single Nanoparticles for Functional Hollow Carbon Nanospheres. *J. Am. Chem. Soc.* **2017**, 139, 13492−13498.

6. X. Zhu; X. Huang; S. Anwer; N. Wang; L. Zhang. Nitrogen-Doped Porous Carbon Nanospheres Activated under Low $ZnCl_2$ Aqueous System: An Electrode for Supercapacitor Applications. *Langmuir* **2020**, 36, 9284−9290.

7. P. Kiany; F. Goharpey; M. Karimi; R. Foudazi. Hybrids of Bowl-like and Crumpled Hollow Carbon Particles Synthesized through Encapsulation Templating. *Langmuir* **2020**, 36,

130−140

8. L. Zhang; L. Liu; X. Hu; Y. Yu; H. Lv; A. Chen. N-Doped Mesoporous Carbon Sheets/Hollow Carbon Spheres Composite for Supercapacitors. *Langmuir* **2018**, 34, 15665−15673.

9. W. Yao; S. He; J. Xu; J. Wang; M. He; Q. Zhang et al. Polypyrrole Nanotube Sponge Host for Stable Lithium-Metal Batteries under Lean Electrolyte Conditions. *ACS Sustainable Chem. Eng.* **2021**, 9, 2543–2551.

10. Fang, Y.; Lv, Y.; Gong, F.; Wu, Z.; Zheng, G.; Zhao, D. et al. Interface Tension-Induced Synthesis of Monodispersed Mesoporous Carbon Hemispheres. *J. Am. Chem. Soc*. **2015**, 137, 2808−2811.

11. Guan, B.; Yu, L.; Lou, X. Formation of Asymmetric Bowl-Like Mesoporous Particles via Emulsion-Induced Interface Anisotropic Assembly. *J. Am. Chem. Soc*. **2016**, 138, 11306−11311.

12. Peng, L.; Hung, T.; Wang, S.; Zhang, X.; Li, W.; Zhao, D. et al. Versatile Nanoemulsion Assembly Approach to Synthesize Functional Mesoporous Carbon Nanospheres with Tunable Pore Sizes and Architectures. *J. Am. Chem. Soc*. **2019**, 141, 7073−7080.

13. Yu, L.; Hu, H.; Wu, H.; Lou, X. Complex Hollow Nanostructures: Synthesis and Energy-Related Applications. *Adv. Mater.* **2017**, 29, 1604563.

14. Zhou, L.; Zhuang, Z.; Zhao, H.; Lin, M.; Zhao, D.; Mai, L. Intricate Hollow Structures: Controlled Synthesis and Applications in Energy Storage and Conversion. *Adv. Mater*. **2017**, 29, 1602914.

15. Liu, H.; Guo, H.; Liu, B.; Liang, M.; Lv, Z.; Sun, X. Few-Layer $MoSe_2$ Nanosheets with Expanded 002. Planes Confined in Hollow Carbon Nanospheres for Ultrahigh-Performance Na-Ion Batteries. *Adv. Funct. Mater*. **2018**, 28, 1707480.

16. Xie, F.; Zhang, L.; Ye, C.; Jaroniec, M.; Qiao, S. The Application of Hollow Structured Anodes for Sodium-Ion Batteries: From Simple to Complex Systems. *Adv. Mater.* **2018**, 31, 1800492.

17. Qiu, D.; Guan, J.; Li, M.; Kang, C.; Wang, F.; Yang, R. Kinetics Enhanced Nitrogen-Doped Hierarchical Porous Hollow Carbon Spheres Boosting Advanced Potassium-Ion Hybrid Capacitors. *Adv. Funct. Mater.* **2019**, 23, 1903496.

18. F. Xu; B. Ding; Y. Qiu; J. Wu; Z. Cheng; H. Wang. Hollow Carbon Nanospheres with Developed Porous Structure and Retained N Doping for Facilitated Electrochemical Energy Storage. *Langmuir* **2019**, 35, 12889−12897.

19. Xu, X.; Asher, S. Synthesis and Utilization of Monodisperse Hollow Polymeric Particles in Photonic Crystals. *J. Am. Chem. Soc.* **2004**, 126, 7940-7945.

20. An, Q.; Qian, J.; Zhao, Q.; Gao, C. Polyacrylonitrile-block-poly methyl acrylate. membranes 2: Swelling behavior and pervaporation performance for separating benzene/cyclohexane. *J. Membr. Sci.* **2008**, 313, 60–67.

21. Okubo, M.; Saito, N.; Fujibayashi, T. Preparation of polystyrene/poly methyl methacrylate. composite particles having a dent. *Colloid Polym. Sci.* **2005**, 283, 691– 698.

22. Huang, Y.; Wang, J.; Zhou, J.; Xu, L.; Song, Y.; Jiang, L. et al. Controllable Synthesis of Latex Particles with Multicavity Structures. *Macromolecules* **2011**, 44, 2404–2409.

23. Tu, Y.; Gu, Y.; Horn, R.; Mitrokhin, M.; Harris, F.; Cheng, Z. A Synthetic Approach Towards Micron-sized Sematic Liquid Crystal Capsules via the Diffusion Controlled Welling Method. *Polym. Chem.* **2015**, 6, 2551-2559.

24. Smith, J.; Meadows, J.; Williams, P. Adsorption of Polyvinylpyrrolidone onto Polystyrene Latices and the Effect on Colloid Stability. *Langmuir.* **1996**, 12, 3773-3778.

25. Shiraishi, Y.; Takii, T.; Hagi, T.; Mori, S.; Ichikawa, S.; Hirai, T. et al. Resorcinol–formaldehyde resins as metal-free semiconductor photocatalysts for solar-tohydrogen peroxide energy conversion. *Nat. Mater*. **2019**, 18, 985–993.

26. Zhu, X.; Xia, Y.; Zhang, X.; Al-Khalaf, A.; Li, W.; Zhao, D. et al. Synthesis of carbon nanotubes@mesoporous carbon core–shell structured electrocatalysts via a molecule-mediated interfacial co-assembly strategy. *J. Mater. Chem. A* **2019**, 7, 8975–8983.

27. Zhang, Z.; Jia, B.; Liu, L.; Zhao, Y.; Qu, X.; Kumar, R. et al. Hollow Multihole Carbon Bowls: A Stress−Release Structure Design for High-Stability and High-Volumetric-Capacity Potassium-Ion Batteries. *ACS Nano* **2019**, 13, 11363−11371.

28. Yang, B.; Liu, S.; Song, H.; Zhou, J. Carbon nanonion-assembled microspheres for excellent gravimetric and volumetric Na-Ion storage. *Carbon* **2019**,153, 298-307.

29. Du, J.; Zhang, Y.; Wu, H.; Hou, S.; Chen, A. N-doped hollow mesoporous carbon spheres by improved dissolution-capture for supercapacitors. *Carbon* **2020**, 156, 523-528.

30. Xu, F.; Ding, B.; Qiu, Y.; Wu, J.; Wei, B.; Wang, H. et al. Hollow Carbon Nanospheres with Developed Porous Structure and Retained N Doping for Facilitated Electrochemical Energy Storage. *Langmuir* **2019**, 35, 12889−12897.

31. Wu, X.; Ding, B.; Zhang, C.; Li, B.; Fan, Z. Self-activation of nitrogen and sulfur dual-doping hierarchical porous carbons for asymmetric supercapacitors with high energy densities. *Carbon* **2019**,153, 225-233.

32. Li, W.; Chen, D.; Li, Z.; Shi, Y.; Wan, Y.; Wang, G.; Jiang, Z.; Zhao, D. Nitrogen-Containing Carbon Spheres With Very Large Uniform Mesopores: The Superior Electrode Materials for EDLC in Organic Electrolyte. *Carbon* **2007**, 45, 1757−1763.

33. Wickramaratne, N. P.; Xu, J.; Wang, M.; Zhu, L.; Dai, L.; Jaroniec, M. Nitrogen Enriched Porous Carbon Spheres: Attractive Materials for Supercapacitor Electrodes and CO_2 Adsorption. *Chem. Mater*. **2014**, 26, 2820−2828.

34. Tian, H.; Lin, Z.; Xu, F.; Zheng, J.; Zhuang, X.; Mai, Y.; Feng, X. Quantitative Control of Pore Size of Mesoporous Carbon Nanospheres through the Self-Assembly of Diblock Copolymer Micelles in Solution. *Small* **2016**, 12, 3155−3163.

35. Zhong, H.; Zhang, H.; Liu, S.; Deng, C.; Wang, M. Nitrogen Enriched Carbon From Melamine Resins with Superior Oxygen Reduction Reaction Activity. *ChemSusChem* **2013**, 6, 807−812.

36. Dattaa, M.; Kumta, P. In situ electrochemical synthesis of lithiated silicon–carbon based composites anode materials for lithium ion batteries. *J. Power Sources* **2009**, 194, 1043–1052.

37. Le, Z.; Liu, F.; Nie, P.; Chen, G.; Wu, H.; Lu, Y. et al. Pseudocapacitive Sodium Storage in Mesoporous Single-Crystal-like TiO_2–Graphene Nanocomposite Enables High-Performance Sodium-Ion Capacitors. *ACS Nano* **2017**, 11, 2952-2960.

38. Xia, Q.; Yang, H.; Wang, M.; Yang, M.; Xia, H.; Yu, Y. High Energy and High Power Lithium-Ion Capacitors Based on Boron and Nitrogen Dual-Doped 3D Carbon Nanofibers as Both Cathode and Anode. *Adv. Energy Mater*. **2017**, 7, 1701336.

39. Niu, J.; Shao, R.; Liu, M.; Dou, M.; Huang, Y.; Wang, F. et al. Porous carbon electrodes with battery-capacitive storage features for high performance Li-ion capacitors. *Energy Storage Mater*. **2018**, 12, 145-152.

40. Zheng, F.; Yang, Y.; Chen, Q. High Lithium Anodic Performance of Highly Nitrogen-Doped Porous Carbon Prepared from a Metal-organic Framework. *Nat. Commun.* **2014**, 5, 5261-5270.

41. Sun, F.; Gao, J.; Liu, X.; Wang, L.; Yang, Y.; Pi, X. et al. High-Energy Li-ion Hybrid Supercapacitor Enabled by a Long Life N-rich Carbon based Anode. *Electrochim. Acta.* **2016**, 213, 626-632.

42. Shao, Y.; El-Kady, M.; Sun, J.; Li, Y.; Zhang, Q.; Kaner, R. et al. Design and Mechanisms of Asymmetric Supercapacitors. *Chem. Rev.* **2018**, 118, 9233-9280.

43. Stoller, M.; Ruoff, R. Best Practice Methods for Determining an Electrode Material's Performance for Ultracapacitors. *Energy Environ. Sci.* **2010**, 3, 1294-1301.

44. Chen, L-F; Huang, Z-H; Liang, H-W; Gao, H-L; Yu, S-H. Three-Dimensional Heteroatom-Doped Carbon Nanofiber Networks Derived from Bacterial Cellulose for Supercapacitors. *Adv. Funct. Mater.* **2014**, 24, 5104-5111.

45. Liu, C.; Zhang, C.; Song, H.; Zhang, C.; Liu, Y.; Cao, G. et al. Mesocrystal MnO Cubes as Anode for Li-ion Capacitors. *Nano Energy* **2016**, 22, 290-300.

46. Jiang, J.; Nie, P.; Ding, B.; Wu, W.; Dou, H.; Zhang, X. et al. Effect of Graphene Modified Cu Current Collector on the Performance of $Li_4Ti_5O_{12}$ Anode for Lithium-Ion Batteries. *ACS Appl. Mater. Interfaces* **2016**, 8, 30926-30932.

47. Li, B.; Dai, F.; Xiao, Q.; Yang, L.; Zhang, C.; Cai, M. et al. Activated Carbon from Biomass Transfer for High-Energy Density Lithium-Ion Supercapacitors. *Adv. Energy Mater.* **2016**, 6, 1600802.

48. Li, S.; Chen, J.; Cui, M.; Cai, G.; Wang, J.; Lee, P. et al. A High-Performance Lithium-Ion Capacitor Based on 2D Nanosheet Materials. *Small* **2017**, 13, 1602893.

49. Dubal, D.; Jayaramulu, K.; Sunil, J.; Narayana, C.; Zbořil, R.; Fischer, R. et al. Metal–Organic Framework MOF. Derived Electrodes with Robust and Fast Lithium Storage for Li-Ion Hybrid Capacitors. *Adv. Funct. Mater.* **2019**, 29, 1900532.

50. Lee, J.; Shin, W.; Ryou, M-H; Jin, J.; Kim, J.; Choi, J. Functionalized Graphene for High Performance Lithium Ion Capacitors. *ChemSusChem.* **2012**, 5, 2328-2333.

51. Yang, Z.; Guo, H.; Li, X.; Wang, Z.; Yan, Z.; Wang, Y. Natural Sisal Fibers Derived Hierarchical Porous Activated Carbon as Capacitive Material in Lithium Ion Capacitor. *J. Power Sources* **2016**, 329, 339-346.

TOC Graphic